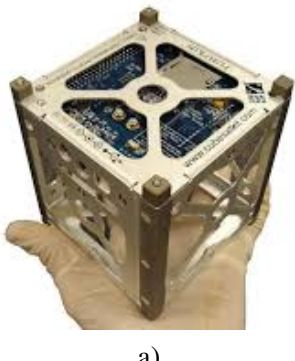


Contents

1	Introduction	2
1.1	Autonomous Rendezvous And Docking	4
1.1.1	Review of existing system	5
1.1.2	Spacecraft Landing Applications	7
1.2	Terrain Mapping and Navigation for a Planetary Exploration Rover	9
1.2.1	Our solution for Korean Lunar Exploration Program	12
1.3	About ISS-gamma mission(can be checked in space)	13
1.4	Outline	13
2	Lidar concept	14
2.1	Submodule	14
3	Design	15
3.1	Laser module	15
3.1.1	Laser	15
3.1.2	Laser collimator	18
3.1.3	Laser driver	23
3.1.4	Completed laser module	24
3.2	MEMS module	25
3.3	SiPM module	27
3.3.1	SiPM detector	27
3.3.2	SiPM collimator	30
3.3.3	Completed SiPM module	31
3.4	Final implementation	32
References		34
Appendix A	Consectetur adipiscing elit	35
A.1	First part	35
A.2	Second	35
Appendix B	Mauris euismod	36

1. Introduction

We are coming to new era of satellites technologies. Artificial satellites come in a variety of sizes ranging from one you can hold in your hand to the size of a school bus. Their dimension and costs are mostly determined by the complexity and type of their instruments (commonly known as payloads). In recent years, thanks to the miniaturization of space technologies, satellites have become smaller for a number of reasons, the first being the cost associated with assembly and launch.



A CubeSat (CS) is a type of miniaturized satellite for space research, these nanosatellites typically weigh between 1 and 10 kilograms and follow the popular 'CubeSat' standard, which defines the outer dimensions of the satellite within multiple cubic units of $10 \times 10 \times 10$ cm.

Fig. 1.1. An example of 1U CubeSat

Utilization of a simplified infrastructure enables a low-cost platform to test the space readiness of new hardware without an exorbitant amount of prohibitive design, thus CSs can help test new instruments or materials and validate their readiness to be integrated into a more complex space mission. The modularity of the CS allows to replace the damaged equipment thereby increasing the duration of the mission. Moreover, the changing the configuration of the modules or adding new ones lead to changing physical characteristics of the system, such as increasing FOV by adding extra-telescope or new wavelength band X-ray/UV/IR, all of these manipulations becomes available right in space. It becomes really easy to organise satellites constellations to enhancing sky coverage. In addition, there is no need thinking about space debris: cubesats burn up in the atmosphere upon re-entry.

One of the areas where CubeSats offer promise is a new type of GRB space observation instrument

that is capable to pick up Gamma Ray Bursts (GRBs) in the hard X-ray to gamma band. GRBs are broadband immense power electromagnetic flashes in space, releases energy, which is typically around 10^{44} J. Observations of GRBs [6,7] play a significant role in understanding these recent discoveries [5,8]. Despite progress in investigations of GRB has been made, especially in the last decade, which culminated in the Fermi and SWIFT missions, up to the moment, some important parameters of GRB, like their prompt emission, still have not been studied well enough. The first direct detections of GWs [1] has brought astronomy into a new era of discovery. The recent coincident detection of a short GRB (by Fermi and other multiwavelength partners) and a Gravitational Wave (GW) trigger has provided concrete proof that at least some short GRBs are produced by binary neutron star mergers [2,3,4,5]. The search for electromagnetic counterparts to GW sources is now more important than ever before. CS are very useful to detect astrophysical counterparts to GW signals as well as other gamma-ray transients, since there are opportunity to enhancing sky coverage for gamma-ray transients that is especially important since GW events can happen anywhere and anytime.

One such project is called BurstCube [11], which will provide localizations which will assist wide-field follow-up observers in afterglow detection and redshift measurement. BurstCube will detect GRBs (long and short) from the entire unocculted sky providing broadband spectra for bursts detected elsewhere, rough localizations for follow-up, and accurately timed light curves.

This thesis is aimed at the development of a common sensor that with a modest design adjustment can meet the needs of both landing and proximity operation Rendezvous and docking applications and also terrain mapping and navigation for a planetary exploration rover.

1.1 Autonomous Rendezvous And Docking

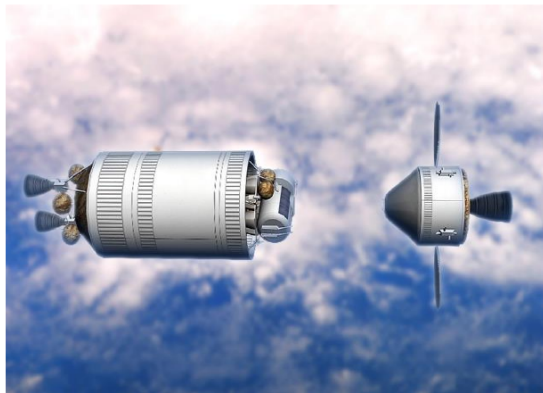


Fig. 1.2. Orion vehicle docking with an Earth Departure Stage

There are also number of space operations that require the ability to rendezvous and dock by an unmanned spacecraft including: servicing satellites on-orbit; assembly of large space structures in Earth orbit; and transfer of Martian soil samples from a lander to a return spacecraft on the Mars orbit, as part of a sample return mission and even space debris removal.

Novel imaging sensors and computer vision technologies are required to detect a target spacecraft at a distance of several kilometers in an arbitrary orientation and to guide the approaching spacecraft to contact with the docking port. The ability to rendezvous and dock with no or minimum human input is considered as an integrated part of CEV (crew exploration vehicle), which is a collection of human and robotic space systems that will allow astronauts to travel safely and cost-effectively to the Moon and Mars. Also this will enable the execution of fuel efficient approach trajectories and reliable operations under any illumination conditions, as well as enabling inspection during fly around and safe station-keeping.

One of the technology that can be used for these purposes is LiDAR: detection and distance measuring method that utilizes pulsed light for measuring the distance towards an object (similar to Radar, but using light instead of radio waves). LIDAR based sensors have gained popularity over RADAR based sensors because of their superior resolution, they also have the advantage of long detection distance and immunity to ambient light over stereo-camera based systems.

Two optical technologies currently used for space rendezvous and docking are cameras and scanning laser rangefinders. The camera based systems typically operate at ranges of up to 100m and the maximum range is limited by a trade-off between the camera image resolution (which is drastically decreasing like square of distance) and field of view, and the size and separation of visual targets. Scanning laser rangefinders use beam steering devices to direct a laser beam to objects in the scene and rely on either a triangulation principle, a measure the phase shift (continuous wave), but the most mature and widely

used LIDAR technology in space operation is pulse laser based TOF (time-of-flight) LIDAR, which measure time between sending and returning of the signal. Emergence of novel LIDAR technologies and computer vision algorithms will lead to a new generation of rendezvous and docking systems in the near future. Such systems will be capable of autonomously detecting a target satellite at a distance of a few kilometers, estimating its bearing, range and relative orientation under virtually any illumination, and in any satellite pose.

The data from the scanning rangefinder must be processed by a vision system to compute the information, such as distance, bearing, pose, that is required by the Guidance, Navigation and Control unit of the autonomous service spacecraft. Some easy to reproduce, semi-analytic calibration approach [A7] is developed for hardware-in-the-loop performance assessment of pose determination algorithms processing point cloud data, collected by imaging a non-cooperative target with LIDARs.

Although laser ranging and scanning sensors are widely used in a variety of industries, a sensor designed for spacecraft operations, including autonomous rendezvous, inspection and servicing remains a challenge. This is primarily due to critical requirements, including the need to have simultaneous high sampling speed, and good range and lateral resolution at both short range of a few meters and at long range of a few hundred meters.

1.1.1 Review of existing system

Up to the present moment, all LiDAR systems used in space are heavy, bulky and have big power consumption, which makes it impossible to use them on the CubeSats. LIDARs flown on Previous Spacecraft: ASC's DragonEye, Ball's Vision Navigation Sensor (VNS), RendezVous Sensor (RVS) / Telegoniometer (TGM) on HTV / ATV, Videometer (VDM) on the ESA Automated Transfer Vehicle (ATV), Trajectory Control Sensor (TCS) on the Space Shuttle. All of them passed the test of time, but replace them came new technologies.

1.1.1.1 The Jena-Optronik RVS Rendezvous and Docking Sensor

The Jena-Optronik RVS Rendezvous and Docking Sensor is the most frequently used LIDAR sensor for docking to the International Space Station ISS. RVS3000 is the advanced 3D imaging LIDAR for rendezvous and docking (Fig. 1.3). Acquisition, tracking and imaging of both cooperative and non-

cooperative targets.

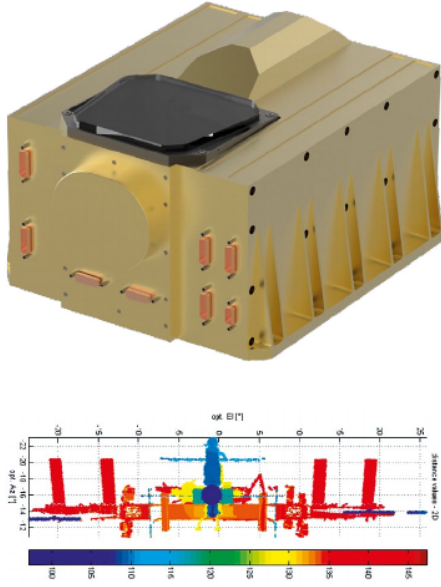


Fig. 1.3. Upper side is RVS3000.
Bottom one is ISS snapshoted by RVS3000.

Field-of-View:	40° x 40°
Wavelength:	910 nm
Operating range against cooperative targets:	< 1500 m
Operating range against non-cooperative targets:	< 250 m
Image frame rate:	up to 2 Hz
Power consumption:	40 W
Dimension:	575 x 569 x 371 mm
Mass:	14.5 kg

Table 1.1. RVS3000 characteristics

Despite the fact that they are leaders in RVS systems, the Lidar has the parameters presented in Table 1.1. Which making this RVS absolutely not applicable for using at small satellites.

1.1.1.2 LIRIS

Another new set of optical sensors for non-cooperative rendezvous and docking, called “LIRIS” (Laser Infra-Red Imaging Sensors) described more detailed in [A9] As part of this project, a prototype for a new 3D Imaging LIDAR was developed, integrated and tested. Fig. 1.4

Same here, dimensions and size (Table 1.2) making this RVS absolutely not applicable for using at small satellites.

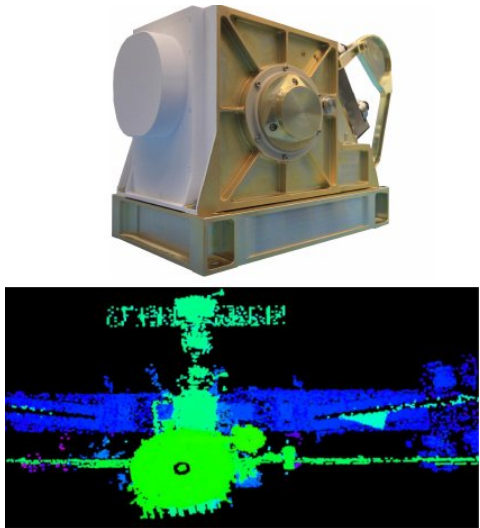


Fig. 1.4. Upper side is LIRIS.
Bottom one is ISS snapshoted by LIRIS.

Field-of-View:	40° x 40°
Wavelength:	1550 nm
Operating range against cooperative targets:	< 3500 m
Operating range against non-cooperative targets:	< 260 m
Image frame rate:	up to 3 Hz
Power consumption:	35 W
Dimension:	292 x 465 x 385 mm
Mass:	13.1 kg

Table 1.2. LIRIS characteristics

1.1.1.3 Neptec's TriDAR

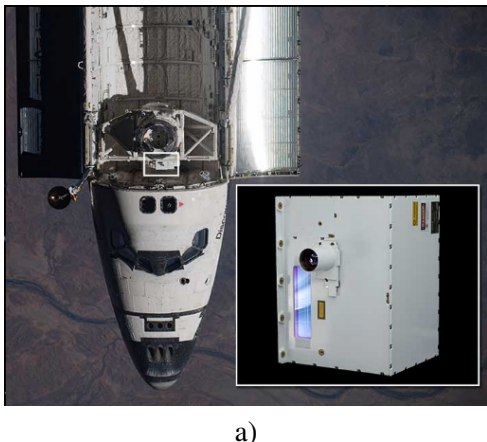


Fig. 1.5. Neptec's TriDAR module

Neptec's TriDAR was specifically designed for non-cooperative missions such as satellite servicing which require high levels of autonomy. This allows the sensor to be adapted to rendezvous and dock to different targets and approach profiles even after launch. Unfortunately, there is no free access to the information about the parameters of the system, but one can say with confidence that they do not exceed RVS3000 / LIRIS, since TriDAR was released much earlier.

1.1.2 Spacecraft Landing Applications

Lidar can be recognized as a primary candidate sensor for safe precision landing on solar system bodies (Moon, Mars, Jupiter and Saturn moons, etc.). For future robotic missions to the Moon and Mars that require landing at pre-designated sites of high scientific value, while avoiding hazardous terrain features, such as escarpments, craters, slopes, and rocks. During the final stages of landing (Approach Phase at fig 1.6), from about 1 km to 500 m above the ground, the lidar can generate 3-dimensional

images of the terrain to identify hazardous features such as craters, rocks, and steep slopes. The onboard flight computer then can use the 3-D map of terrain to guide the vehicle to a safe location.

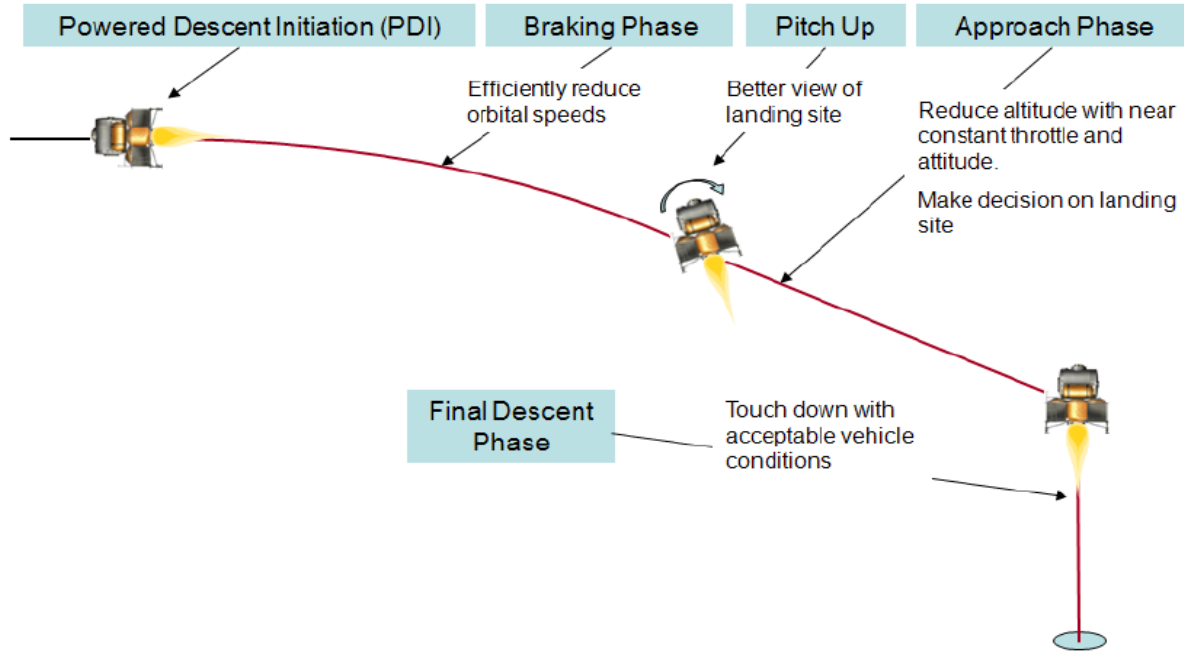
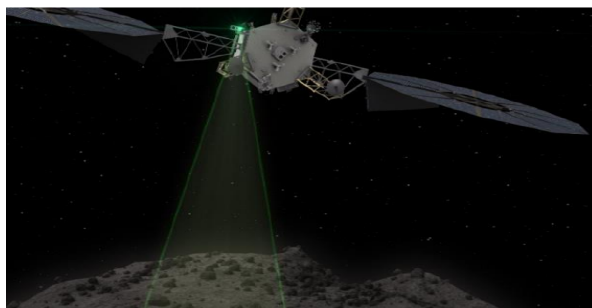


Fig. 1.6. Typical Lunar descent and landing phase

According to [A8, A2], the minimum requirements which should be satisfied in lidar system are represented in Table 1.4:



Range:	0 to 5000 m
Field of View:	> 20° x 20°
Spatial Resolution:	<0.25m at 300m
Range accuracy:	<5m(5km) <0.1m (300m) <0.02m (10m)
Image frame rate:	> 1Hz

Fig. 1.7. Lidar sensor characterizing an asteroid surface before terminal approach for collecting samples or capturing a boulder

Table 1.3. The minimum requirements which should be satisfied in lidar system for landing

One more application comes from studying of morphological characterization of asteroids, the lidar can analyze asteroid surface before terminal approach (Fig. 1.7).

1.1.2.1 Our solution for Rendezvous And Docking

Advance of sensor technologies and novel tracking algorithms has led to a few new approaches of autonomous rendezvous and dock, but it still typically requires multiple systems to complete the operation. It is desirable to have one system that can do the tracking at all distances. Reducing the number of sensors necessary to cover the required range of distances (preferably to one) has significant benefits due the reduced launch mass and volume, and lower power requirements.

At our Laboratory we have developed such vision system based on a scanning LIDAR to get real-time 3D picture. Our LiDAR consumes much less power (5W) and has an incredible small mass (<500g) and size of a matchbox, while is able to track satellite pose with high accuracy and high frame rate.

1.2 Terrain Mapping and Navigation for a Planetary Exploration Rover

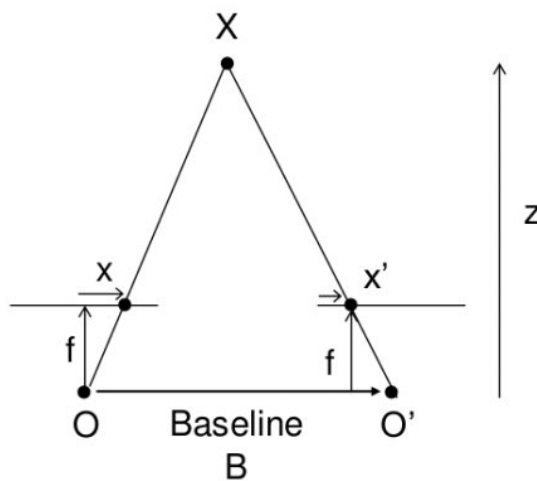
In recent decades, terrain modelling and reconstruction techniques have increased research interest in precise short and long distance autonomous navigation, localisation and mapping within field robotics. One of the most challenging applications is in relation to autonomous planetary exploration using mobile robots. Rover navigation on planetary surfaces can be extremely hazardous, which includes vehicle rollover on sloped terrain, or immobilizing wheel slippage on loose sand. That is why high resolution topographic data is required to ensure rover safety and mission success. A terrain feature information can be exploited to assess obstacle size, slope angle, or terrain roughness so that the rover is able to find its heading for travel.

The farther an explored planet is, the longer it would take a commanding signal to reach from an earth commanding station to planet exploring rover. Thus, it is necessary for a space rover to be capable of autonomous and semi-autonomous decision making such as localization, navigation, and environmental mapping, with little intervention from ground control at very high traverse speeds. Missions that require absolute rover localisation remain a challenging problem due to the absence of helping technologies such as Global Positioning Systems (GPS) on extraterrestrial planets.

The majority of the rover onboard vision systems in past and current missions (such as, Mars Exploration Rover (MER), Mars Science Laboratory (MSL) and Exobiology on Mars (ExoMars)) use cameras for terrain perception, such as; stereopsis for autonomous rover navigation (e.g., visual odometry), hazard

detection (e.g., slip perception) and scientific study (e.g., MSL ChemCam) [5]

The drawbacks of the camera-based terrain mapping are that a stereo matching process is generally a time-consuming task(finding correlation between 2 frames of cameras) for the low-power flight CPU of the rover, requiring relatively long computational time, especially higher resolution cameras are used. [3]. Additionally, the quality of visual information may vary with the intensity of sunlight/shadows. Also, there is a significant decrease in the accuracy of the estimated depth Z with the increase in distance from the camera (Eq. 1.2), which may not be deemed suitable for long range terrain modelling and perception.



The left diagram contains equivalent triangles. Writing their equivalent equations will yield us following result:

$$z = f \cdot \frac{B}{d} \quad (1.1)$$

Where f is focal length, B is baseline, $d = x - x'$. Here d is known as the disparity.

Fig. 1.8. A simple stereo geometry

From Eq 1.1 by differentiating, for depth error we got:

$$\delta z = \frac{z^2}{f \cdot B} \cdot \delta d \quad (1.2)$$

As can be seen from Eq. 1.2 depth resolution is proportional to the square of the depth (Z) and is inversely proportional to the focal length (f) and baseline (B), or distance between the cameras. Good depth resolution requires a large baseline (B) value, a large focal length (f) value and a small depth (Z) value. Depth resolution depends on accurate disparity estimations. The accuracy of disparity estimation is directly proportional to pixel size, where smaller pixel sizes provide better resolution. Typically, disparity can be estimated accurately to about one fifth of a pixel. For a camera with a pixel size of 7.5 microns, this translates to a disparity resolution of 1.5 microns.

Hence stereopsis does not provide an optimal solution beyond a few metres from the rover for future

more challenging planetary rover missions.

Another technique for the terrain mapping involves the use of a lidar that can determine a distance from a laser emitter to an object based on the time of flight principle, this technology been used extensively for precise long and short target detection, identification, and depth estimation. Extensive research and development for using the LIDAR technique in a terrain feature mapping and terrain classification described in [5]–[8]. Comparing the LIDAR-based terrain mapping to the camera-based one, the LIDAR can directly measure three-dimensional distances from the sensor to the objects, providing “point cloud” data of the scene without any additional processes (the camera-based mapping needs stereo matching for the 3D mapping). After that, the point cloud data of the terrain features provided by the LIDAR are converted into a digital elevation map with a sector-shaped reference grid for the DEM conversion, termed as C^2DEM .

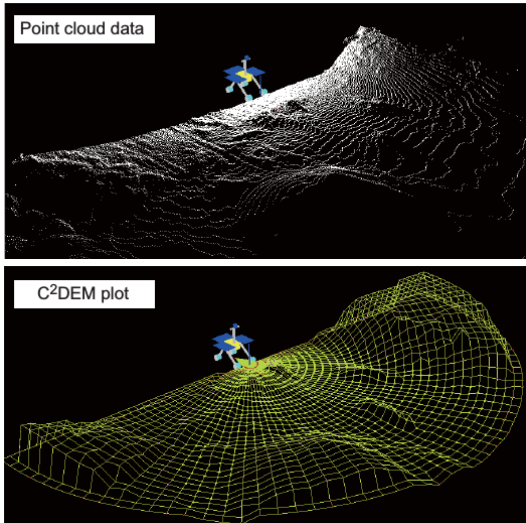


Fig. 1.9. An example of point cloud to C^2DEM transformation.

An example of C^2DEM conversion from a point cloud data is shown in Fig. 1.9. The terrain mapping with the C^2DEM achieves detailed representation of the terrain near the rover as well as wide selectivity of the rover look-ahead directions. Finally, the path planning algorithm considering three indices: terrain inclination, terrain roughness, and path length makes decision about the path.

Lidar-based terrain mapping and navigation for a planetary exploration rover was successfully tested in [ISA2012] by using motorable lidar made by Hokuyo. Vision system of this rover uses both stereo-cameras and lidar placed at 2-axis rotatable fimbale (Fig.1.10).

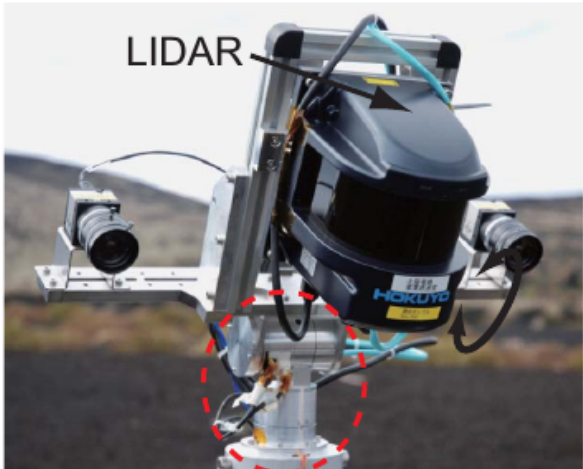


Fig. 1.10. Gimbaled-LIDAR system for terrain mapping.

Scanning range:	0.1 to 30m
Wavelength:	905 nm
Field of View:	20° x 190°
Scanning angle resolution:	0.25°
Range accuracy:	± 0.1 m
Image frame rate:	> 1Hz
Power consumption:	6 W
Dimensions:	124 x 126 x 150mm
Weight:	800 g

Table 1.4. Specification of the LIDAR scanning system

Clearly that LiDAR has a key-role in rover navigation, it covers both short range and long range. Additionally to be easy-to use and therefore adapted to fast-making decisions, like multi-path planning that is used for an autonomous mobility of a planetary exploration rover. The data allows cm-precise estimations of distances, heights and slopes, which are critical for safe rover displacement as well as remote and contact science operations. It also allows extremely detailed surface mapping of objects and therefore has implications for our knowledge of planetary surfaces. A drawback of the LIDAR-based mapping is that the LIDAR cannot obtain pure color data of the terrain (in grayscale or RGB) even though it can measure the distance as well as intensity of the light reflected from objects. Therefore, a possible future realization will be forwarded to enables three-dimensional mapping with color of the terrain.

1.2.1 Our solution for Korean Lunar Exploration Program

Our laboratory developed a LiDAR submodule with the size of a matchbox. This LiDAR consumes little power and has a small mass. The LiDAR submodule (or a set of several submodules) is suitable for close distance scanning, and it is perfect for Mars and Lunar rovers because it can allow them to make detailed scans of the surrounding without considerable payload losses. The concept we are developing (MEMS pinhole), basically, is a unique technology that allows not only LiDARs development, but also other scientific instruments, such as spectrometers or cameras. Thus, our lidar can be easily integrated for the Korean Lunar Exploration Program for use in a lunar rover.

1.3 About ISS-gamma mission(can be checked in space)

Preflight test can be done in ISS gamma exp (we can detect trash to check wheter it working or not).

1.4 Outline

This thesis is organized as follows. In chapter 2, I describe

2. Lidar concept

picture with modules

2.1 Submodule

3. Design

3.1 Laser module

3.1.1 Laser

3.1.1.1 The requirements

The laser plays one of the key role in the whole system. Strict requirements are imposed on it, starting from the pulse energy, ending with the generation stability. The maximum distance at which we can detect an object directly depends on the pulse energy, in our case the energy should be more than 1uJ to reach 200m distance. To get a picture in good pixel resolution, especially at high FPS, we need a fairly fast pulse repetition rate, at least 10kHz. Using the TOF method it is extremely important to have a small pulse width, the smaller, the smaller the measurement error and the higher the accuracy. To obtain acceptable accuracy, the pulse width should be less than 10 ns and have a Gaussian-like shape, moreover timing jitter should be as small as possible. The wavelength of the laser should coincide with the receiver spectrum for better amplification, in the case of SiPM it is around 420 nm. Being used in space, reability, size and power consumption become critical.

Finaly, the requirments for laser is:

Pulse energy:	$\geq 1 \text{ uJ}$
Repetition rate:	$\geq 10 \text{ kHz}$
Pulse duration:	$\leq 10 \text{ ns}$
Wavelength, λ :	depends on SNR, <1000nm
Power consumption:	$\leq 2 \text{ W}$
Dimension:	$\leq 3 \text{ cm}^3$

Table 3.1. Requirements for the laser system

3.1.1.2 Theoretical background

Nowadays, there are a lot of laser solutions: Solid-state lasers, Semiconductor lasers, Fiber lasers, Gas lasers, but many of them do not meet all our requirements. Solid-state lasers can be used in a pulsed mode with Q-switching (active or passive) technique and also in Mode-locking mode. In the case of the Mode-locking mode, the repetition frequency can reach many MHz, whereas the pulse duration is much lower: typically between 30 fs and 30 ps. Despite the complexity of creation such laser, the energy of the pulse, is extremely small and can not be used for our purposes.

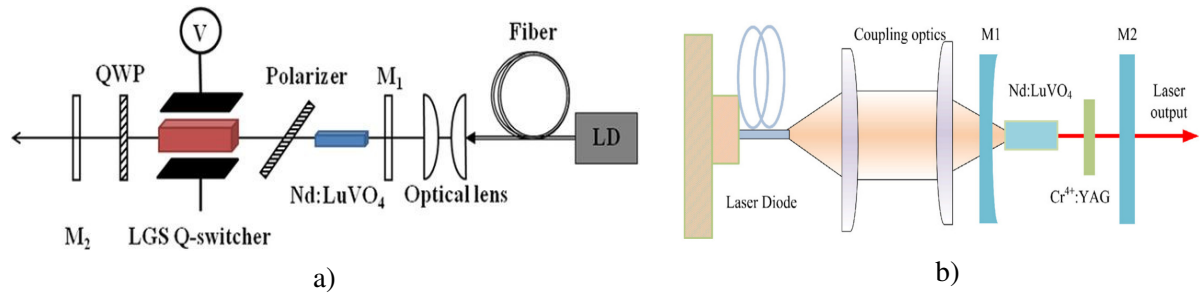


Fig. 3.1. Typical Q-switched schemes for active and passive mode: a) Laser diode end-pumped actively Q-switched laser utilizing a langasite (LGS) crystal as an electro-optic Q-switch. b) High repetition rate laser-diode end-pumped passively Q-Switched Nd:LuVO₄/Cr⁴⁺:YAG

In case of Q-switched lasers (Fig. 3.1), the pulse repetition rate is typically in the range from 1–100 kHz, sometimes higher. Passively Q-switched microchip lasers have reached pulse durations far below 1 ns and repetition rates up to several megahertz, whereas large (typically amplified) laser systems can deliver pulses with many kilojoules of energy and durations in the nanosecond range. For active Q-switching, the losses are modulated with an active control element (active Q-switch), typically either an acousto-optic or electro-optic modulator. Here, the pulse is formed shortly after an electrical trigger signal arrives. There are also mechanical Q-switches such as spinning mirrors, used as end mirrors of laser resonators. In any case, the achieved pulse energy and pulse duration depends on the energy stored in the gain medium, i.e. on the pump power and the pulse repetition rate. For passive Q-switching (sometimes called self Q-switching), the losses are automatically modulated with a saturable absorber. Here, the pulse is formed as soon as the energy stored in the gain medium (and thus the gain) has reached a sufficiently high level. In many cases, the pulse energy and duration are then fixed, and changes of the pump power only influence the pulse repetition rate. Compared with active Q-switching, passive Q-switching is simple, takes up little space and cost-effective (eliminating the modulator and its

electronics), and is suitable for very high pulse repetition rates. However, the pulse energies are typically lower. Unfortunately, closest for our wavelength interest are based on a neodymium-doped laser crystal which are applicable for Q-switching lay in the wavelength range ~ 1 um, such as Nd:YVO₄/Cr⁴⁺:YAG 914 nm [1][2], Nd:GdVO₄/Cr⁴⁺:YAG 912 nm [3][4], Nd:LuVO₄/Cr⁴⁺:YAG 916 nm [5]. Due to the size of laser system, the best solution is passive Q-switched microchip laser: alignment-free monolithic solid-state laser where the laser crystal (or glass) is directly contacted with the end mirrors of the laser resonator (Fig. 3.2).

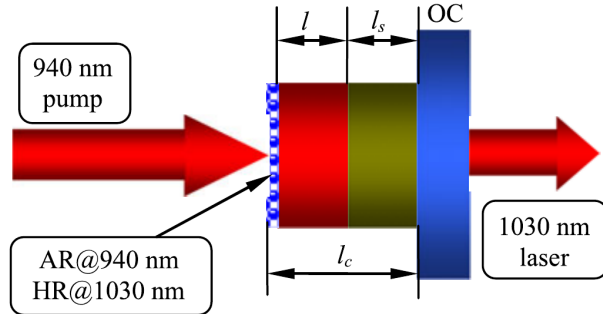


Fig. 3.2. The experimental setup of laser-diode pumped Yb:YAG/Cr:4+:YAG composite ceramics passively Q-switched laser. OC is the output coupler.

Q-switched microchip lasers also allow the generation of unusually short pulses with durations below 1 ns, in extreme cases even below 100 ps. This holds particularly for passive Q switching with a SESAM [2], but it is also possible to use a saturable absorber crystal e.g. of Cr:YAG or some Cr-doped ceramics [1].

3.1.1.3 The laser choice

Eventually according to numerical simulation [1,2] the minimum pump power for high-repetition laser system, which is satisfied our requirements is quite big $> 6\text{-}8\text{W}$ this is just for start trigger lasing at 10kHz (for Nd:YVO₄/Cr⁴⁺ with best transmission parameters). This is because, optical-to-optical efficiencies – typically of the order of 5-20%. At the same time, electrical-to-optical efficiencies sometimes even above 60%.

Therefore, we are trying to use a laser diode. Fortunately there is powerful high-repetition rate laser diode with quite short pulse duration $\sim 10\text{ns}$ at 905 nm from OSRAM Opto Semiconductors (Fig. 3.3).



Fig. 3.3. Osram laser diode

Peak output power:	75 ± 10 W
Forward current:	40 A
Repetition rate:	~ 100 kHz
Pulse duration:	≥ 10 ns
Emission wavelength, λ :	905 ± 10 nm
Rise time:	1 ns
Fall time:	1 ns
Emmiting area:	200 x 10 um
Beam divergence:	25° x 9°
Operating temperature:	-40 .. 100 °C

Table 3.2. OSRAM Laser diode characteristics

Despite the fact that the amplification of the detector at this wavelength is small, the laser power exceeds these losses, moreover at this wavelength the noise is smaller. Also it is eye-safe, that expand spectrum of possible applications.

3.1.2 Laser collimator

3.1.2.1 Analytical calculations

Radiation characteristic of laser diode features carries due to its small size, light quality, low threshold, low cost, these properties the laser diode play an important role in the information time, especially in the field of communication LIDAR. Optical system is an essential part, which plays an important role in decreasing the divergence angle and homogenizing the beam spot which have an immense influence on the light signal back from the target. Together with the detector's collimator, a system with high resolution and high SNR can be obtained. The design of the system was done by using ZEMAX model which also includes shaping and zooming features of design model.

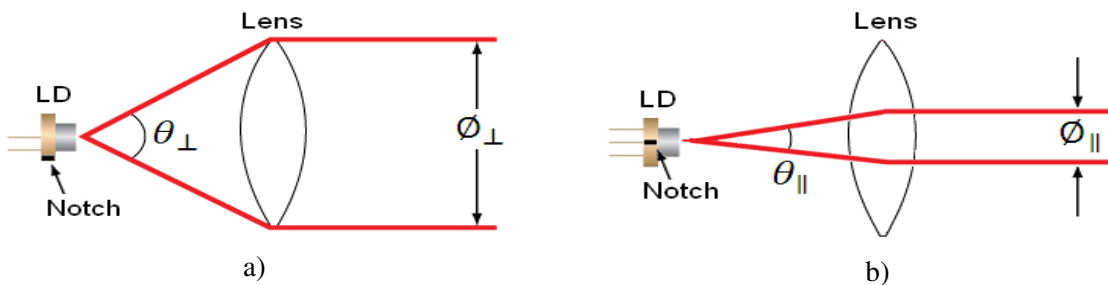


Fig. 3.4. In the above schematics, LD denotes the laser diode, \mathcal{O}_{\parallel} and \mathcal{O}_{\perp} are the beam diameters in the parallel and perpendicular orientations, respectively, and θ_{\parallel} and θ_{\perp} are the divergence angles in the parallel and perpendicular orientations, respectively.

a) Perpendicular beam divergence from laser diode. b) Parallel beam divergence from laser diode.

The beam divergences of an edge-emitting laser diode will be different in the parallel and perpendicular directions, leading to an elliptical beam (Fig. 3.4). This can be compensated for by inserting anamorphic prism pairs or cylindrical lenses into the collimated beam, but in our case it's not needed.

Since the output of a laser diode is highly divergent, collimating optics are necessary. Traditional spherical lenses have a simple shape that can be described as an arc of a circle and can be specified using only a radius of curvature. Although these lenses are simple to manufacture and inexpensive to use, they suffer in performance due to a phenomenon called spherical aberration. This inherent defect is due to the fact that a spherical shape is not the ideal shape for a focusing or collimating lens to be. The ideal case is a more complex shape that is typically defined using a radius of curvature, a parabolic term (conic), and several high order coefficients. The complex shape of aspheric lenses allows for correction of spherical aberration. This provides better quality collimated beams for collimating applications, a smaller spot size for focusing applications, and better image quality for imaging applications. In fact, in many cases just a single aspheric lens can take the place of several conventional spherical lenses, leading to a lighter, more compact, less expensive, and better performing optical system. Aspheres are now a viable design option for many applications. Choosing an appropriate aspheric lens for collimating a laser diode is essential, as the resulting beam size and transmission range are dependent on the lens used.

To calculate the beam size of a collimated laser diode, we first need to know its divergences and area of emitting surface. The specifications for the OSRAM laser diode indicate that the perpendicular and parallel beam divergences are 25° and 9° , respectively. Because of this asymmetry in the two axes, an elliptical beam will form as the light diverges. To collect as much light as possible during the collimation process, consider the larger of these two divergence angles in any calculations (i.e. 25°).

In paraxial approximation, for beam diameter calculation after passing lens the following formula is using (Fig. 3.4):

$$\varnothing_{\perp} = 2 \cdot f \cdot \tan\left(\frac{\theta_{\perp}}{2}\right) \quad (3.1)$$

For beam divergence after passing the optical system (Fig. 3.5):

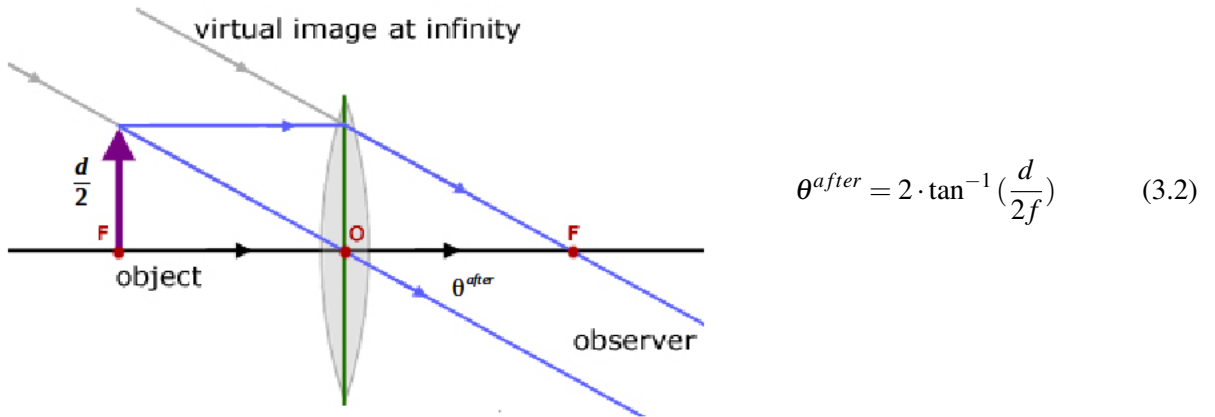


Fig. 3.5. Simple demonstration, shows divergence of the beam emitted from object, seated at the focus of the optical system. Here, d is the size of emitting area of laser diode (200 μm in our case), f is total focal length of the optical system.

From the formulas 3.1 3.3, it is obvious that the larger the focal lens, the larger the diameter of the beam and the smaller the beam divergence. It means, that by increasing focal length we can achieve the desirable level of divergence (up to diffraction limit, with assumption we free of aberrations). But, by increasing focal length the beam diameter is also increased. Since the size of MEMS is only 3.5 mm, we have limitation for focal length (we want reflect all light which are emitted). The same result can be getting from the Lagrange invariant relationship between the heights and angles of any two rays propagating through the system (in case of linearity of paraxial optics).

Important to note, that even a well-collimated beam has a non-vanishing divergence because of wave-nature of the light, the beam diameter varies (for large distances) with the distance from the laser diode collimator. The resulting beam divergences of the collimated beam:

$$\theta_{\perp/\parallel} = \frac{2 \cdot \lambda}{\pi \cdot \varnothing_{\perp/\parallel}} \quad (3.3)$$

3.1.2.2 The optical system choice

According to formula 3.1, our focal length should be ~ 6.5 mm. The first way is just using nearest suitable aspherical lens, which has focal length 6.2 mm (Fig. 3.22). These laser molded aspheric lense fulfilled all our the needs. Also, this aspheric lens is anti-reflection coated for optimum transmission in the 600 - 1050 nm wavelength range. The anti-reflection coating provides <0.4% average reflection over



Fig. 3.6. Aspheric lens used for laser collimator

Effective Focal length:	6.2 mm
Clear Aperture:	3.7 mm
Numerical aperture (NA):	0.3
Material:	D-ZK3
Center Thickness:	3.484 mm
Coating:	BBAR (600 - 1050 nm)

Table 3.3. Aspheric lens characteristics

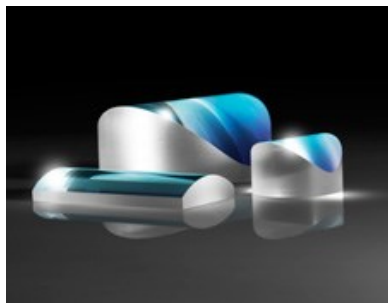


Fig. 3.7. Two cylindrical lens used for laser collimator

Effective Focal length:	8 mm	12 mm
Clear Aperture:	4 mm	5.4 mm
Numerical aperture (NA):	0.31	0.25
Material:	N-BK7	N-BK7
Center Thickness:	3 mm	2.2 mm
Coating:	BBAR (600 - 1050 nm)	12 mm

Table 3.4. Two cylindrical lens characteristics (for each axis)

the entire design wavelength range. By utilizing a single aspheric lens, the need for a multi-lens system is eliminated, allowing for a more compact and robust design.

The second way is using two cylindrical lenses for each axis separately (Fig. 3.7). This allows the use of a lens with a large focal length, because the divergence of the parallel axis is 9° , not 25° .

3.1.2.3 ZEMAX simulation

Once the analytical calculations are completed, and the system variables are determined, the ZEMAX optical design program is used to simulate a specific example. ZEMAX is a design software containing features and tools to design, optimize, and analyze any optical system.

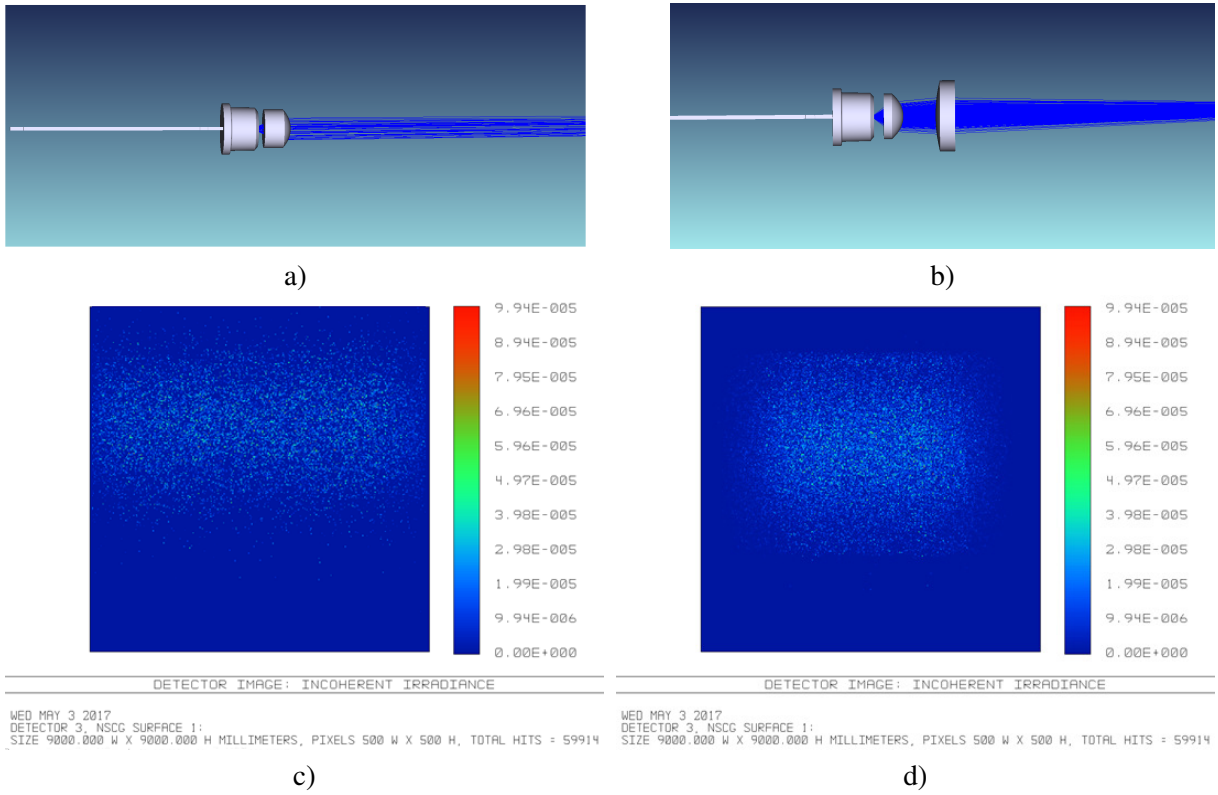


Fig. 3.8. The ray tracing and also beam spots results are obtained using non-sequential Zemax mode, the laser diode was simulated based on real ray-data file (5M rays) from OSRAM site. a) The ray traycing for sinle-lens collimator. b) The ray traycing for two-lens collimator. c) Spot diagram for sinle-lens collimator. d) Spot diagram for two-lens collimator.

The ray tracing results obtained using ZEMAX are presented in (Fig. 3.8.a)) for the single-lens system and in (Fig. 3.8.b)) for the two-lens system. Beam spots obtained with ZEMAX are presented in (Fig. 3.8.c)) and (Fig. 3.8.d)) for the single-lens and two-lens systems, respectively. As can be seen, in the case of a system of two lenses, the beam has a smaller divergence, as expected. But, a first design method seems to be more practical than the second one, since there is only one lens, and it might be easier to align a single-lens system than to align a two-lens system. However, the two-lens system has more degrees of freedom, and therefore, the optical parameters can be more widely adjusted. Also considering the size of it, it may get bulky and hard to use. Therefore, as a compact collimator a single-lens collimator used, whose length is 10 mm, and diameter 6 mm.

The simulation results verify the availability that the beam from the laser diode meets the requirements after optical emission from system. Simulation was also made in a sequential mode just in case (Fig. 3.9).

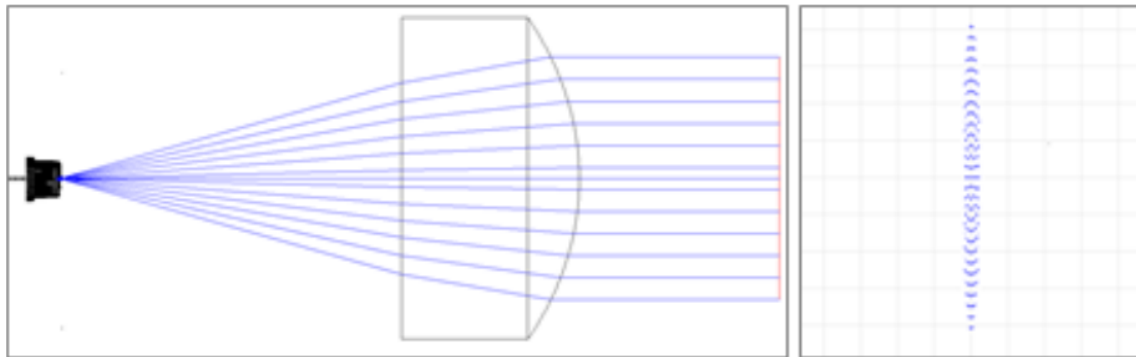


Fig. 3.9. Ray-tracing of single-lens collimator based on aspheric lens in sequential mode

3.1.2.4 Assembled laser collimator

As a result, the assembled compact laser collimator with an integrated OSRAM diode is shown in the Fig. 3.10. This colimator provide beam angular size is $0.1^\circ \times 2.5^\circ$, by having length only 10 mm, and diameter 6 mm.



Fig. 3.10. Assembled compact laser collimator

3.1.3 Laser driver

To operate Osram laser diode the laser driver is required. The LDP-AV 40-70 is the smallest available source for nanosecond pulses (Fig 3.11). It provides 40A with fixed pulse duration of 5 ns at repetition rate up to 100kHz.

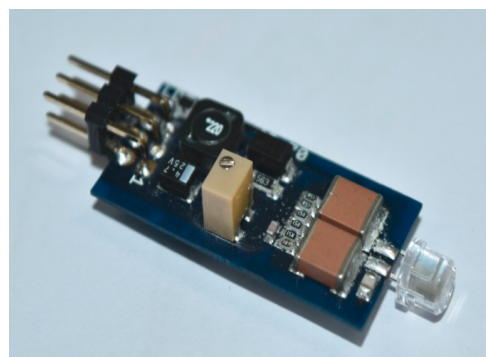


Fig. 3.11. Commercial laser driver with attached Osram diode.

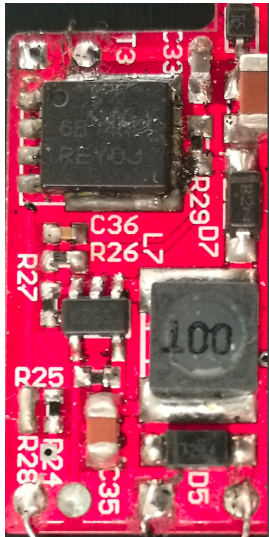


Fig. 3.12. Our laser driver.

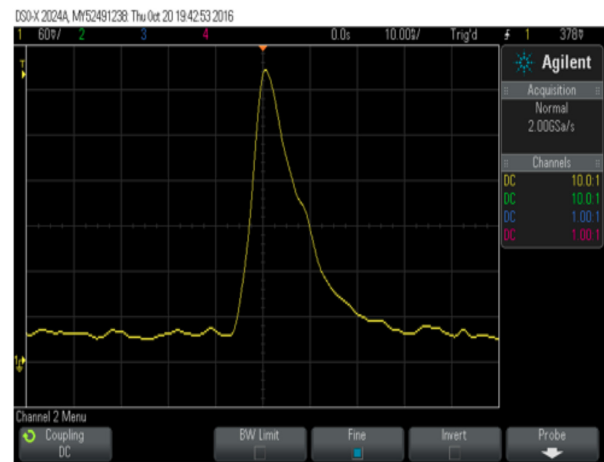


Fig. 3.13. Output of detector caught by 2GSa/s oscilloscope after laser shoot.

Our team made an analog of this laser driver, smaller in size with the same characteristics. The device optimized for size and functionality (Fig. 3.12).

Figure 3.13 shows the screenshot of the 2Gsa/s oscilloscope, as can be seen, the pulse duration is of the order of 10 ns. The detector was SiPM which is described in the next section.

3.1.4 Completed laser module

Finally we got laser system with the following params:

Pulse energy:	~ 1 uJ
Repetition rate:	12 kHz
Pulse duration:	≤ 10 ns
Wavelength, λ :	905 nm
Power consumption:	≤ 0.25 W
Dimension:	≤ 3 cm³

Table 3.5. Characteristics of the laser system

The repetition rate is tunable parameter, it was chosen in consideration of low power consumption and obtaining a good enough pixels resolution.

3.2 MEMS module

MirrorcleTech's MEMS micromirror technology provide ultra low-power and very fast optical beam scanning in two-axes. Gimbal-less Two-Axis Scanning Micromirror Devices based on ARI-MEMS fabrication technology are highly versatile and adaptable to various applications. The devices deflect laser beams to optical scanning angles of up to 30° at high speeds in both axes.

Schematic diagram of MEMS mirror is shown in Fig. 3.14. Each actuator can utilize electrostatic rotators of arbitrary length, arbitrarily stiff linkages, and arbitrarily positioned mechanical rotation transformers. In addition, the device can have an arbitrarily large mirror diameter.

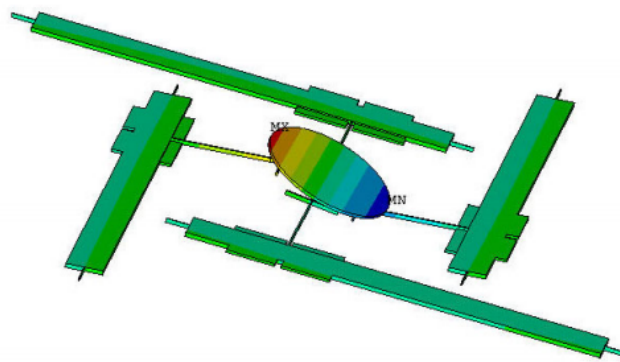


Fig. 3.14. Schematic diagram of an example of Mirrorcle's proprietary gimbal-less two-axis scanning actuator based on four electrostatic bidirectional rotators connected to the central stage by special silicon linkages.

Most of Mirrorcle MEMS mirrors can be operated over a very wide bandwidth from dc (they maintain position at constant voltage with nearly zero power consumption at the device) to several thousand Hertz. Such fast and broadband capability allows nearly arbitrary waveforms such as vector graphics, constant velocity line scanning, point-to-point step scanning, object tracking, etc.

There is a one-to-one correspondence of actuation voltages and resulting angles: it is highly repeatable with no detectable degradation over time. Positional precision of mechanical tilt in open loop driving of the mirror actuators is at least 14 bits (16384 positions) on each axis. This is in great part due to the electrostatic drive methodology and singlecrystal silicon material selection.

Despite that most of the modern LiDARs are based on motor scanning, MEMS mirrors are commonly used in LiDARs too. The advantage of using MEMS mirror instead of a motor is the significant decrease

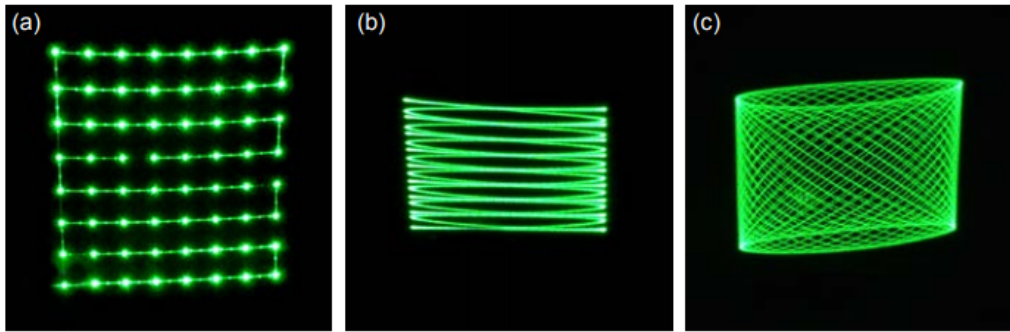


Fig. 3.15. Examples of trajectories in (a) point-to-point scanning mode (quasistatic), (b) resonant scanning mode on the x-axis (sinusoidal beam motion) and quasi-static on the y-axis (triangle wave motion), and (c) resonant scanning mode on both axes, showing a 2D resonant Lissajous pattern.

of LiDAR's size and mass in comparison. However, there are disadvantages like a small FOV (order of 20° instead of 360° in case of rotating) and a small receiver aperture, which is limited by the size of the MEMS mirror. There is trade-off between the size of the mirror, speed and scan angle. Devices with larger-diameter mirrors are correspondingly have smaller scanning angle and also scanning speed is slower due to the increased inertia, which are fourth power of radius. Thus, the scanning speed reduces quadratically with increase of mirror size. The bonded mirrors methodology allows to select the size, as well as the geometry of mirrors for each individual application, in order to optimize the trade-offs between speed, beam size, and scan angle.

To operate MEMS mirror the driver is needed. Digital Input MEMS Driver - PicoAmp 5.X, suggested by Mirrocle, was significantly redesigned, changing the size more than 2 times. It has low voltage supply and low power consumption (<100mW). There are 4 unipolar analog outputs 0V-200V (X+, X-, Y-, Y+), which are used for the control of MEMS mirror via SPI commands to 16-bit DAC. There are also ability to set any cut-off frequency for Embedded Bessel low pass filter by providing external clock signal.

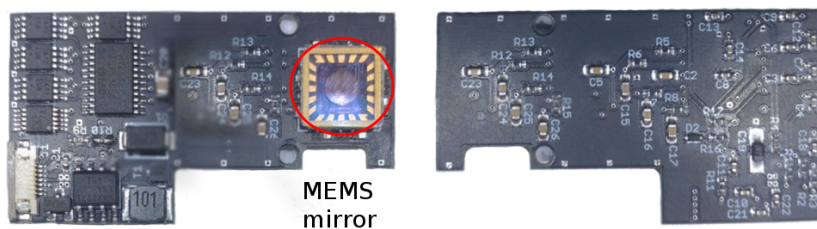


Fig. 3.16. Upper and lower side of MEMS PCB.

For our purpose the MEMS with 3.6 mm diameter was chosen. Already attached to the MEMS driver board the mirror is shown in the figure 3.16. The MEMS mirror characteristic are presented in

table 3.17. Important to note, that optical deflection angle by X-axis will be twice bigger.

This diameter of selected MEMS mirror is good enough to make possible good collimation of laser beam. The scanning FOV will be $25^\circ \times 13^\circ$. The resonant frequency is enough to perform scanning at 12 FPS with 8 lines (Fig. 3.15 a)).

Diameter:	3.6 mm
Scanning angle - X axis:	6.6°
Scanning angle - Y axis:	6.5°
Resonant frequency - X axis:	303 Hz
Resonant frequency - Y axis:	300 Hz

Fig. 3.17. Mirocle's MEMS mirror characteristics

3.3 SiPM module

3.3.1 SiPM detector

The Silicon Photomultiplier (SiPM) is a single-photon sensitive sensor that has performance characteristics comparable to a conventional ICCD/PMT/APD (Table 3.18). with the practical advantages of a solid-state sensor.

	ICCD	PMT	APD	SiPM
Sensitivity	~ 10 ph.e	1 ph.e	~ 10 ph.e	1 ph.e
Gain	$10^3 - 10^6$	10^6	100-200	10^6
Dynamic Range	large	$\sim 10^3$	large	$\sim 10^3/mm^2$
Operating Voltage	$\sim 100V$	1-2 kV	100-500 V	20-50 V
Efficiency at blue	50%	20%	50%	30%
Timing	$\sim 1ms$	$\sim 100ps$	$\sim ns$	$\sim 30ps$

Fig. 3.18. Specification of the LIDAR scanning system

It is formed of a summed array of closely-packed Single Photon Avalanche Photodiode (SPAD) sensors (Fig. 3.19)

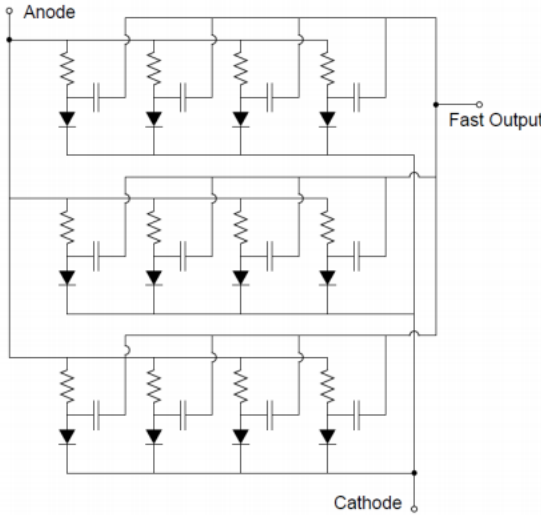


Fig. 3.19. An SiPM consists of an array of microcells (SPAD plus quench resistor) with summed output.

The SiPM is operated in Geiger-mode which enables high gain (1×10^6), high detection efficiency (>50%) and fast timing (sub-ns rise times) at moderate bias (30V). This is achieved by creating a high field region in the diode that generates a self-perpetuating charge avalanche when a photon is absorbed. Passive quenching, is achieved through the use of a series resistor which limits the current drawn by the diode during breakdown. This lowers the reverse voltage seen by the diode to a value below its breakdown voltage, thus halting the avalanche. The diode then recharges back to the bias voltage, and is available to detect subsequent photons.

Since the capacitance of the microcell will depend upon its area, the reset time will vary for different microcell sizes, with a 50mm microcell SiPM having a significantly longer reset time and gain than a 10mm microcell SiPM. Another one of the most important parameter is PDE (Photon Detection Efficiency). This is the product of the $QE \cdot AIP \cdot FF$, where QE is quantum efficiency, AIP is the avalanche initiation probability and FF is the fill factor of the microcells. The characteristics and PDE graph of the selected SiPM detector by Sensl are shown in the table 3.6 and figure 3.26 correspondingly.

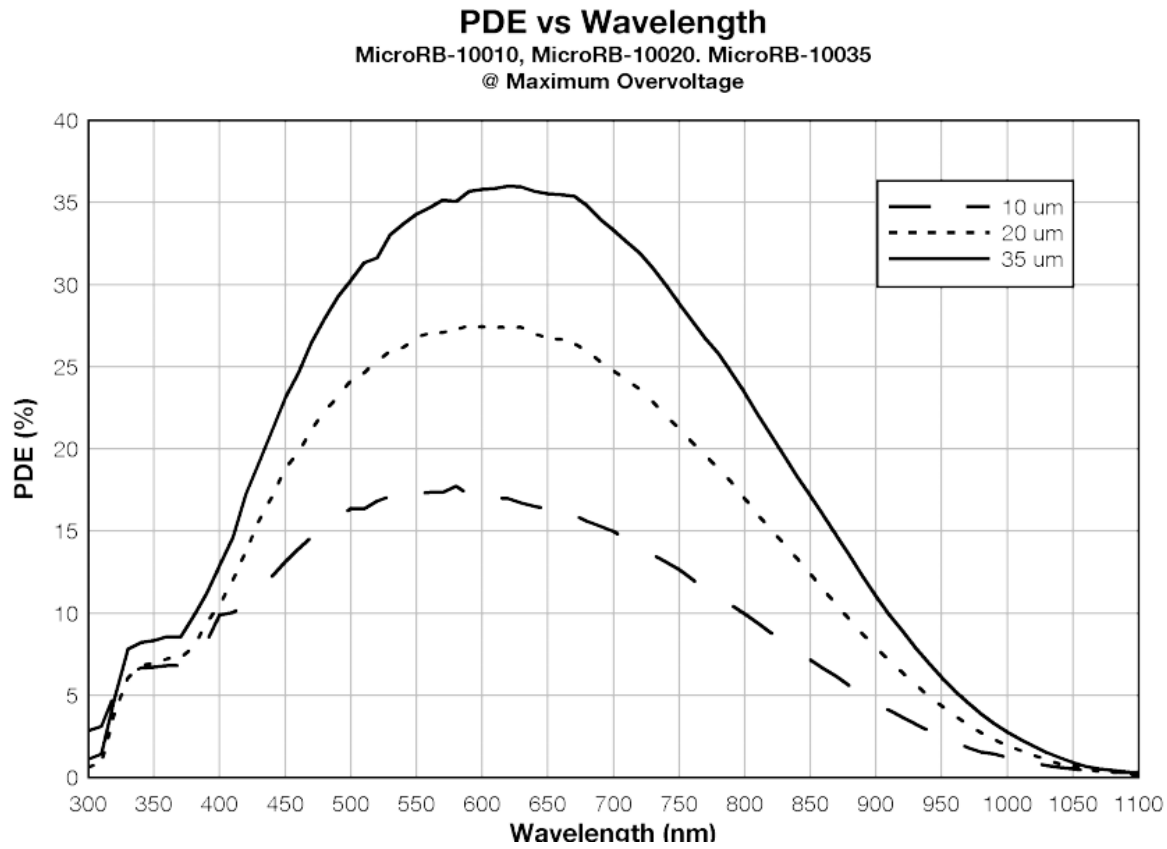


Fig. 3.20. PDE for different cell sizes.

Microcell size:	35 um
Gain:	$1.7 \cdot 10^6$
PDE @ 905 nm:	$\leq 10\%$
Dark current rate:	3.8 MHz
Dark current:	1.5 uA
Rise time:	3.7 ns
Recharge time:	73 ns

Table 3.6. Characteristics of the SiPM

In accordance with the characteristics of the detector, we can say that it is ideally suited for the LiDAR based on TOF technology. High gain and small rise time allows single-detection mode with high SNR, while small recharge time allows very high repetition rate, up to 10MHz.

Figure 3.26 shows the SiPM experimental setup (left) and screenshot of the SiPM output after laser shooting (right), caught by the 2Gsa/s oscilloscope.

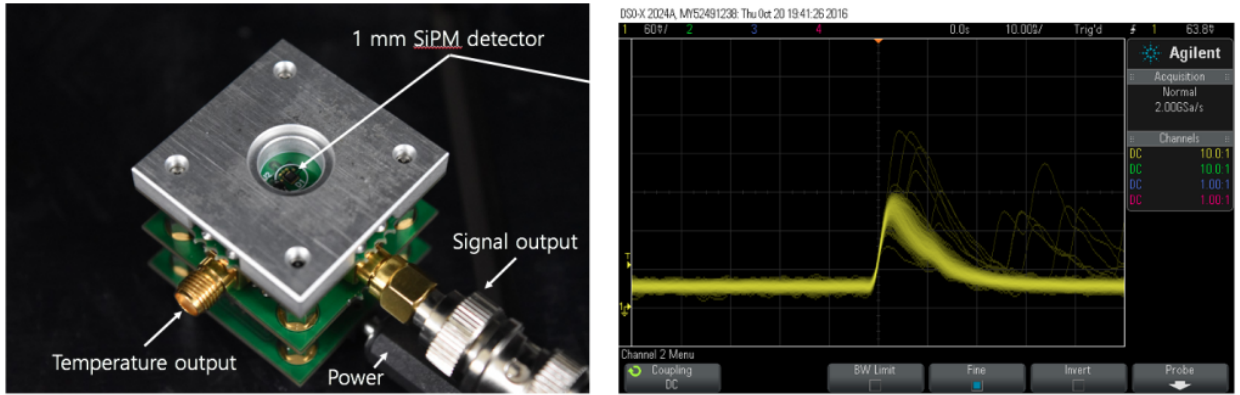


Fig. 3.21. SiPM experimental setup (left) and output of SiPM after laser shooting (right).

3.3.2 SiPM collimator

Receiver optics is one of the most important in the whole system. It provides a specified FOV, minimizing noise. Our receiver aperture is limited by diameter of the MEMS, so it should not exceed 3.6mm. Since we don't need wide FOV we are not suffering so much due to aberrations, thus the optical system consists of one aspherical lens to focus received signal to SiPM and a pinhole for cutting FOV according to eq:3.4. FOV of SiPM should be big enough to cover laser beam, but at the same time should be quite small to decrease noise impact.

$$FOV = 2 \cdot \tan^{-1} \left(\frac{d}{2 \cdot f} \right) \quad (3.4)$$

Where d is pinhole size, f is focal length.



Fig. 3.22. Aspheric lens used for SiPM collimator.

Pinhole size:	200 um
Effective Focal length:	4.5 mm
Clear Aperture:	3.7 mm
Numerical aperture (NA):	0.3
Material:	D-ZK3
Center Thickness:	3.484 mm
Coating:	BBAR (600 - 1050 nm)

Table 3.7. Characteristics of optics for SiPM, bandpass filter should be improved.

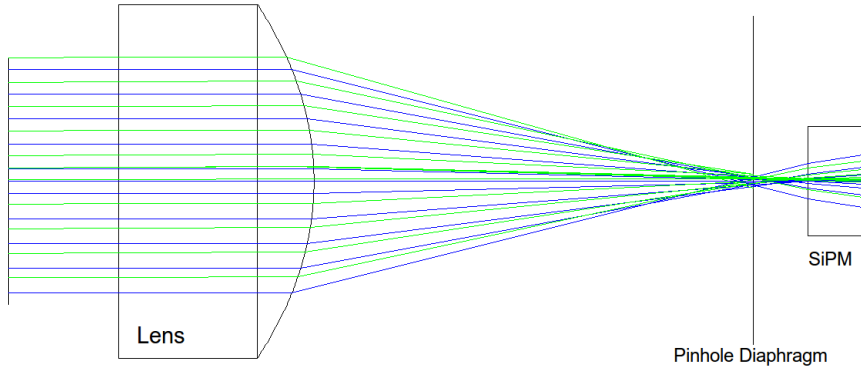


Fig. 3.23. Zemax simulation of SiPM collimator.

According Zemax simulation, the FOV will be $2.8^\circ \times 2.8^\circ$, thus we have tolerance for match both laser FoV and SiPM to cover fast axis of laser beam ($0.1^\circ \times 2.5^\circ$).

3.3.3 Completed SiPM module

The finished SiPM PCB is shown in the figure 3.24. It consists of readout electronics for SiPM, laser driver and TDC chip.

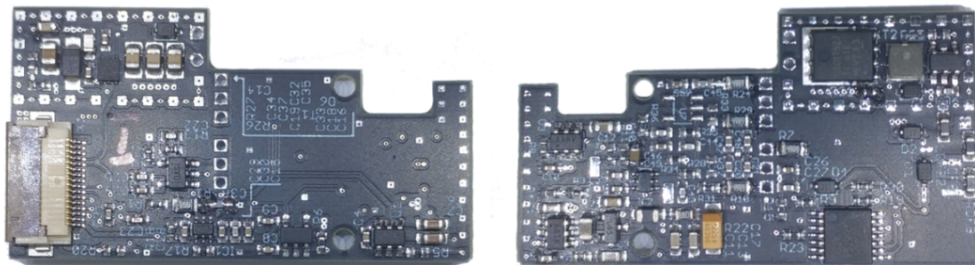


Fig. 3.24. Upper and lower side of SiPM PCB.

The assembled SiPM collimator with already attached SiPM to the bottom of tube is shown in figure 3.25.



Fig. 3.25. Assembled SiPM collimator with integrated SiPM.

3.4 Final implementation

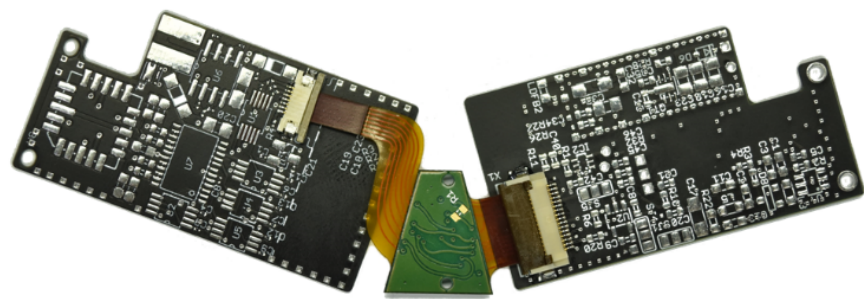


Fig. 3.26. Zemax simulation of SiPM collimator.

Picture of real submodule here

AZAZAZA Their long-term aid [1] [2]

The Latex typesetting markup language is specially suitable for documents that include mathematics.

Formulas are rendered properly and easily once one gets used to the commands.

Given a set of numbers, there are elementary methods to compute its Greatest Common Divisor, which is abbreviated GCD. This process is similar to that used for the Least Common Multiple (LCM).

References

- [1] L. Haggarty and B. Pepin. An investigation of mathematics textbooks and their use in english, french and german classrooms. *Proceedings of the British Society for Research into Learning Mathematics*, 21(2):117–125, 2001.
- [2] L. Haggarty and B. Pepin. An investigation of mathematics textbooks and their use in english, french and german classrooms. *Proceedings of the British Society for Research into Learning Mathematics*, 21(2):117–125, 2001.

A. Consectetur adipiscing elit

A.1 First part

asxdsdsda

A.2 Second

I'm a second part!

B. Mauris euismod

??